Scripta Materialia 159 (2019) 89–93

Contents lists available at ScienceDirect

Scripta Materialia

journal homepage: www.elsevier.com/locate/scriptamat

Excellent mechanical and corrosion properties of austenitic stainless steel with a unique crystallographic lamellar microstructure via selective laser melting

Shi-Hai Sun [a,b,1], Takuya Ishimoto [a,b,1], Koji Hagihara [b,c], Yusuke Tsutsumi [d], Takao Hanawa [d], Takayoshi Nakano [a,b,*]

[a] Division of Materials and Manufacturing Science, Graduate School of Engineering, Osaka University, 2-1 Yamadaoka, Suita, Osaka 565-0871, Japan
[b] Anisotropic Design & Additive Manufacturing Research Center, Osaka University, 2-1 Yamadaoka, Suita, Osaka 565-0871, Japan
[c] Department of Adaptive Machine Systems, Graduate School of Engineering, Osaka University, 2-1 Yamadaoka, Suita, Osaka 565-0871, Japan
[d] Department of Metallic Biomaterials, Institute of Biomaterials and Bioengineering, Tokyo Medical and Dental University, 2-3-10 Kanda-Surugadai, Chiyoda, Tokyo 101-0062, Japan

ARTICLE INFO

Article history:
Received 25 July 2018
Received in revised form 5 September 2018
Accepted 12 September 2018
Available online xxxx

Keywords:
Additive manufacturing
Selective laser melting
Texture
Lamellae
316L stainless steel

ABSTRACT

We first developed a unique "crystallographic lamellar microstructure" (CLM), in which two differently oriented grains appear alternately, in a 316L stainless steel specimen via selective laser melting technology. The CLM was composed of major ⟨011⟩ grains and minor ⟨001⟩ grains aligned along the build direction, which stemmed from vertical and approximately ±45° inclined columnar cells formed in the central and side parts of melt-pools, respectively. The development of CLM was found to largely improve the material properties via the strengthening of the product, simultaneously showing superior corrosion resistance to commercially obtained specimens.

Crystallographic texture control has recently gained great interest in the study of additive manufacturing (AM) [1–8]. Highly texturized materials with preferential crystallographic orientations can feature mechanical anisotropies in Young's modulus [7], yield stress [2], fatigue resistance [9], creep resistance [10], etc. Therefore, crystallographic texture control, including the formation of single-crystalline textures, is believed to be an important strategy in the development of materials with superior mechanical properties through AM. The scan strategy is indicated to have an impact on texture evolution in AM, and different scan strategies lead to distinguished crystallographic orientations [5–8].

Efforts made to control crystallographic texture through AM have generated single-crystalline-like and fiber-type textures in some kinds of metallic materials [1–8]. Under a certain scan strategy, the formation of a microstructure with a single orientation is ubiquitous; however, microstructures with combinations of multiple orientations have not yet been realized, despite the fact that many materials with controlled microstructures, for example lamellar microstructures composed of different phases [11,12], show superior mechanical properties. In the present study, by utilizing selective laser melting (SLM; a powder bed fusion process), we developed a unique texture in 316L stainless steel, in which two differently oriented grains appear alternately. This unique texture is hereafter referred to as a "crystallographic lamellar microstructure" (CLM). In this paper, the detailed microstructural characteristics, mechanical properties, and corrosion resistivity—which are fundamentally expected of 316L stainless steel as a structural material—will be clarified, by comparing a specimen with CLM to that with a single-crystalline-like microstructure fabricated by SLM, as well as commercially available plate material.

Gas atomized 316L stainless steel powder was obtained from EOS GmbH (Germany) for use in the experiment. The nominal composition of the powder was 18Cr-14Ni-2.5Mo-0.03C (wt%), and the powder size was under 53 μm. SLM was conducted using an EOS M 290 3D printer by the "X-scan strategy", i.e., the laser beam was scanned bidirectionally along the *x*-axis without rotation (Supplementary Fig. 1). In this study, the laser scanning direction and build direction in SLM were defined as the *x*- and *z*-axes, respectively. By controlling the energy density, we found the optimal fabrication parameters for eliminating porosity and developing crystallographic textures: fabrication under a relatively low energy density resulted in a CLM; that under a relatively high energy density resulted in a single-crystalline-like texture. Although we focused on the unique CLM in this study, the single-crystalline-like texture formation via SLM is also novel in 316L stainless steel; therefore, 316L stainless steel plate material fabricated by standard industrial

* Corresponding author at: Division of Materials and Manufacturing Science, Graduate School of Engineering, Osaka University, 2-1 Yamadaoka, Suita, Osaka 565-0871, Japan.
E-mail address: nakano@mat.eng.osaka-u.ac.jp (T. Nakano).
[1] These authors contributed equally to this work.

https://doi.org/10.1016/j.scriptamat.2018.09.017

processes (Yakin Kawasaki, Japan) was used as an additional reference material. Products of 10 mm × 10 mm × 10 mm were fabricated for microstructure observation and corrosion tests, and those of 10 mm × 10 mm × 30 mm were fabricated for preparing tensile specimens with a gauge of 5 mm length, 1.5 mm width, and 0.8 mm thickness, as described previously [13]. To avoid unexpected heat effects from neighbor specimen melting, we ensured that there was sufficient distance between the specimens in the SLM fabrication process.

The microstructure was observed by scanning electron microscopy (SEM; JEOL JIB-4610F, Japan) following etching, and the texture development was examined by electron backscatter diffraction (EBSD) pattern analysis via SEM. Tensile tests were conducted in vacuum at room temperature with an initial strain rate of 1.67×10^{-4} s^{-1}. The loading orientation and thickness direction were set to be parallel to the *z*- and *x*-axes, respectively. To evaluate the corrosion resistance, anodic polarization measurements (linear sweep voltammetry) were performed in a 0.9 wt% NaCl aqueous solution with a potentiostat (HABF-501G, Hokuto Denko, Japan) and a function generator (HB-111, Hokuto Denko, Japan). A saturated calomel electrode (SCE) and Pt plate were used as a reference and counter electrode, respectively. The specimens were mechanically ground to #800 grit SiC abrasive paper. After immersing the specimens into the test solution at 37 °C, a gradient anodic potential was applied at a constant sweep rate of 1 mV s^{-1}. The exposed area of the specimen contacting the electrolyte was 0.35 cm^2 (6.7 mm in diameter).

The mechanical and corrosion tests were performed on three specimens in each condition ($N = 3$), and the quantitative data are given as mean ± standard deviation (SD). Comparisons between the means were statistically performed using one-way analysis of variance (ANOVA) and post hoc Tukey HSD tests (IBM SPSS Statistics 25). A value of $P < 0.05$ was considered statistically significant.

The relative densities measured by Archimedes' method were 99.6% and 99.4% for the specimens fabricated under the lower and higher energy densities, respectively, demonstrating that these optimized conditions resulted in almost fully dense specimens. Fig. 1(a, b) show inverse pole figure (IPF) maps illustrating the crystallographic texture of the specimens, observed along the *x*-, *y*-, and *z*-directions. In the specimen fabricated under higher energy density, a single-crystalline-like texture was confirmed to be developed, in which ⟨011⟩ and ⟨100⟩ were aligned nearly parallel to the build and scanning directions, respectively, as in a recent report using β-Ti with a body-centered cubic (bcc) structure [7]. On the other hand, the crystal orientation map for the specimen fabricated under lower energy density showed a characteristic lamellar pattern, despite the fact that the specimen was confirmed to be composed of a face-centered cubic (fcc) single-phase. That is, a unique CLM, in which two kinds of layers with different orientations were stacked alternately along the *y*-axis, was found to be developed.

For detailed characterization of the CLM, the misorientation angle variation along the line AB (indicated in Fig. 1(a)) is displayed in Fig. 1(c). Large misorientation angles, expressed as sharp peaks, represent

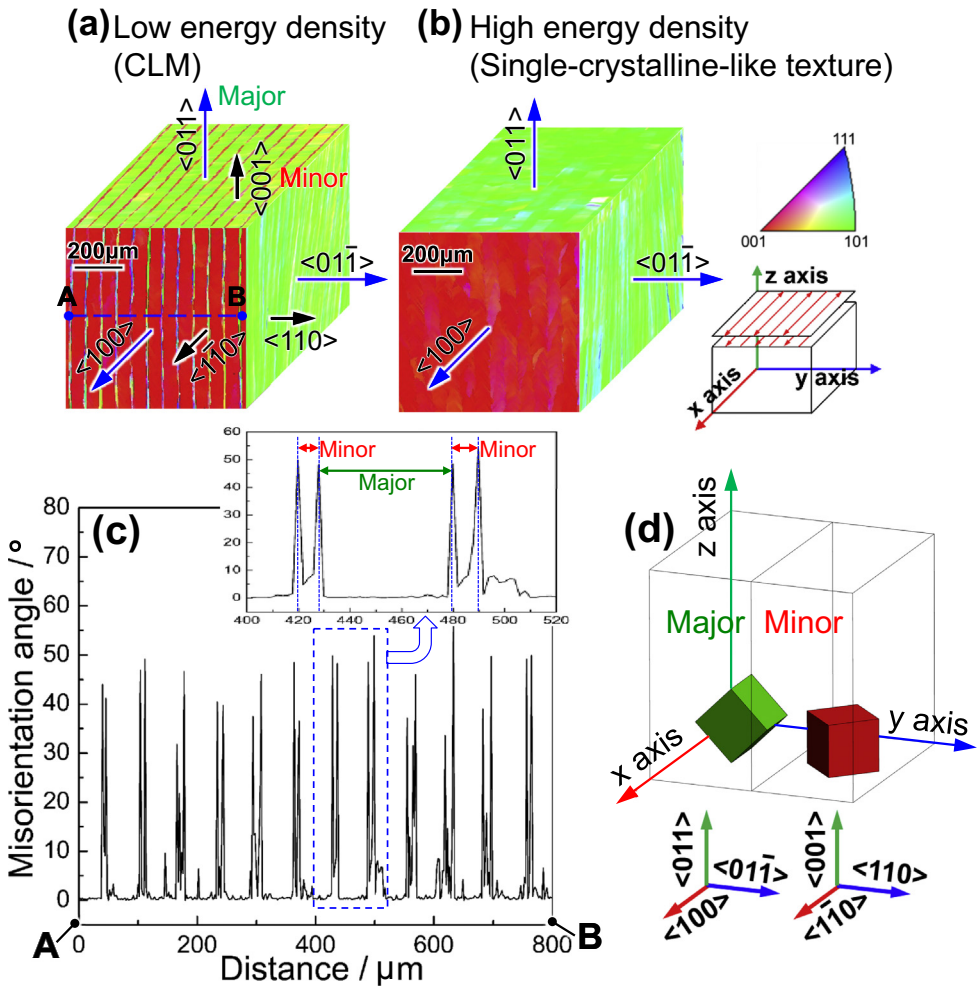

Fig. 1. Crystal orientation maps in the specimens fabricated in X-scan strategy with (a) low energy density and (b) high energy density, observed along the *x*-, *y*- and *z*-directions, respectively, taken by SEM-EBSD. (c) Misorientation angle variation along line AB in (a). (d) Schematic illustration showing the crystallographic orientation relationship between major and minor layers in the CLM formed under low energy density.

boundaries between major (wide) and minor (narrow) layers. The average widths of the major and minor layers, i.e., the regions sandwiched by the peaks, were measured to be 55.1 ± 3.6 μm and 10.4 ± 2.8 μm, respectively. The average misorientation angle between the major and minor layers was 44.2 ± 6.3°. Taken together with the IPF map analysis, the predominate crystallographic orientation relationship between the two layers was determined as follows:

In x-axis : Major $\langle 100 \rangle$ // Minor $\langle 1\bar{1}0 \rangle$

In y-axis : Major $\langle 01\bar{1} \rangle$ // Minor $\langle 110 \rangle$

In z-axis : Major $\langle 011 \rangle$ // Minor $\langle 001 \rangle$

This orientation relationship is shown schematically in Fig. 1(d). The texture in the major layer is the same as that observed in the single-crystalline-like specimens shown in Fig. 1(b), but the minor layer is rotated by 90° along the y-axis.

To clarify the microstructure and crystallographic orientation at the melt-pool level, SEM and EBSD analyses were conducted on the yz-plane, i.e., along the X-scanning direction. Fig. 2(a, b) show SEM images of the built product displaying the shape of melt-pools, and enlarged SEM images are shown in Fig. 2(a′, b′). Note that the observation was conducted at the top layer of the built product, to examine the shape of the melt-pool without the influence of subsequent repetitive heating, which is a distinctive feature of layer-by-layer fabrication. Fig. 2(c, d) show the corresponding IPF maps along the z-axis. The observed melt-pool traces were highlighted with black lines in the images. The melt-pool shape in the specimen fabricated under higher energy density was deeper and more shouldered than when fabricated under lower energy density (Fig. 2(b)).

Different cellular-type solidification microstructures were observed in the melt-pools of the two specimens. In the specimen fabricated under lower energy density (Fig. 2(a, a′, c)), columnar cells had developed along an incline of approximately ±45° with respect to the build direction (green arrows), accompanied by elongated cells parallel to the build direction (red arrows) at the center of the melt-pools (Fig. 2(a, a′)). On the other hand, the specimen fabricated under higher energy density (Fig. 2(b, b′, d)) showed ±45°-oriented cells (green arrows) only. The direction of the elongated cellular microstructure almost corresponds to ⟨001⟩, as determined by the locally created pole figures (Fig. 2(e, f, g)). As such, the ⟨001⟩ direction in each grain was examined, and is indicated by arrows in the figures. This clearly demonstrates that the vertical and approximately ±45° inclined columnar cells in the central and side parts of melt-pools lead to the formation of the CLM with ⟨011⟩ + ⟨001⟩ orientation along the build direction. The cellular microstructure and the resultant crystal orientation were inherited across the layers, demonstrating that the texture development was governed by epitaxial growth. Epitaxial growth has been reported to be a major solidification behavior in many other fcc metals [1,8] during the SLM process; however, the formation of a CLM is quite unique.

The SLM-fabricated CLM specimen exhibited excellent mechanical properties and corrosion resistance. Fig. 3 shows the true stress–true strain curves obtained by the tensile tests and polarization curves measured in 0.9 wt% NaCl aqueous solution. The results of a reference specimen, which was fabricated by standard industrial processes, are also displayed for comparison. The reference material showed a grain size of ~9 μm and no specific texture, as shown in Supplementary Fig. 2. The SLM specimens displayed much higher yield stress (0.2% proof stress) and significantly larger elongation than the reference specimen, demonstrating the superiority of the specimens fabricated by SLM in this study. Moreover, the specimen with CLM had a significantly higher yield stress (by around 12%) than the specimen with single-crystalline-like microstructure, as shown in Table 1. It is thought that the boundaries between major and minor layers may hinder the transmission of dislocations, leading to enhanced yield stress in the specimen with CLM.

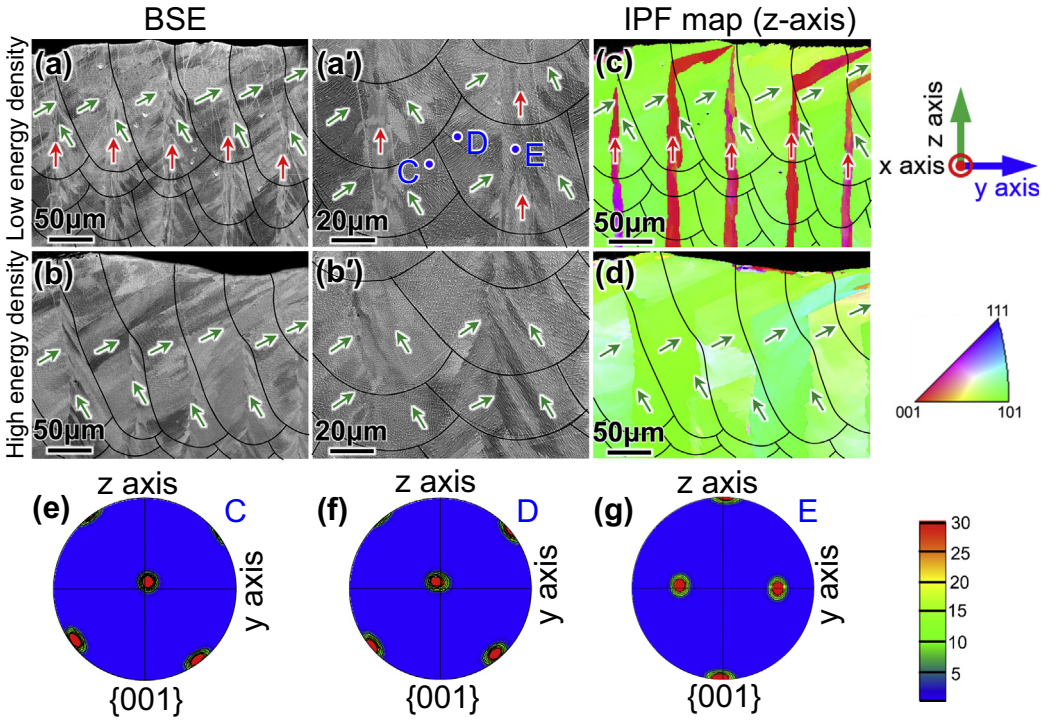

Fig. 2. (a, b) Backscattered electron (BSE) images showing the morphologies of the boundaries of the columnar cells and the traces of melt-pools observed on the yz-plane, in the specimens fabricated with (a) low energy density and (b) high energy density. (a′, b′) Higher magnification images of (a, b). (c, d) Corresponding crystal orientation maps along the z-axis. (e, f, g) {001} pole figures taken at points C, D, and E in (a′), respectively. Arrows indicate the direction of cell elongation (green: ±45°-oriented cells; red: vertically-oriented cells). (For interpretation of the references to color in this figure legend, the reader is referred to the web version of this article.)

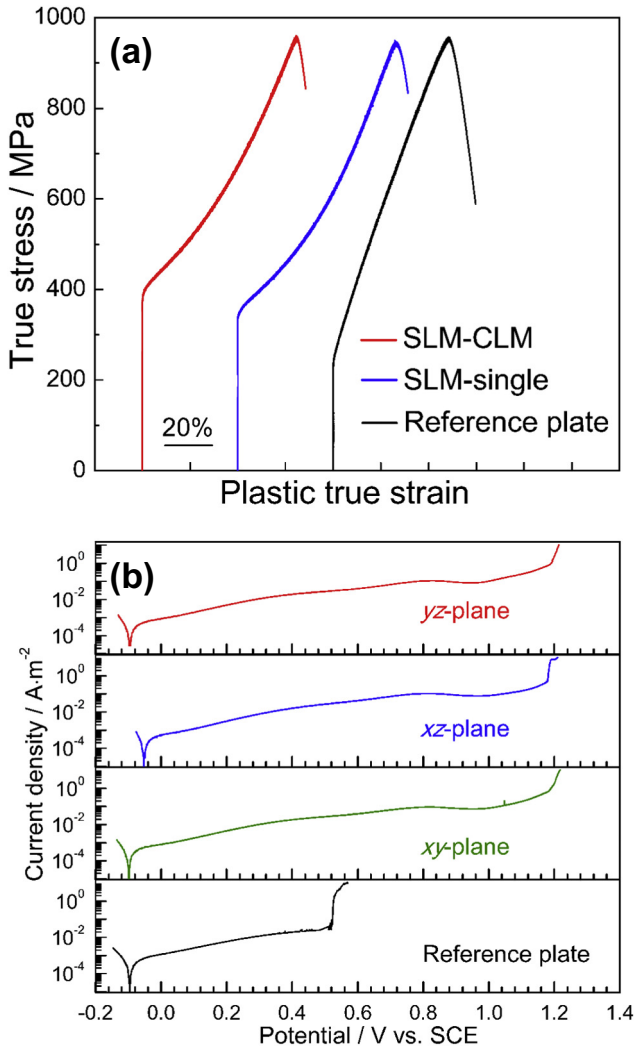

Fig. 3. (a) True stress–true strain curves of the specimens fabricated with different energy density in tensile tests at RT, and (b) potentiodynamic polarization curves of the SLM-fabricated CLM specimen measured in 0.9 wt% NaCl aqueous solution at 310 K, together with that of commercially obtained plate specimen.

Corrosion tests were performed on the SLM-fabricated CLM specimen. It was expected to show inferior corrosion resistance owing to the presence of grain (layer) boundaries, which generally tend to act as initiation sites of pitting corrosion. Surprisingly, however, the breakdown potentials were extremely high, at over 1.2 V in all tested planes in the SLM-fabricated CLM specimen, compared to the breakdown potential of ~0.5 V in the reference specimen. It has been reported that SLM improves the corrosion resistance of 316L stainless steel [14], however, to the authors' best knowledge, no breakdown potential over 1 V has been reported. The breakdown potential of 1.2 V is around the transpassive state in which chromium oxide is thermodynamically unstable, indicating that the SLM process contributes to this ultimate corrosion resistant potential of 316L stainless steel, although the underlying mechanisms remain unclear.

In these ways, the development of a CLM by suitable control of the SLM fabrication process was proven to be highly beneficial regarding the strength of 316L stainless steel, and simultaneously revealed extremely high corrosion resistance. The development of a single-crystalline-like texture with ⟨011⟩ orientation along the build direction by the X-scan strategy has been well-documented previously [7,8]. Thus, only the formation of the minor layer with ⟨001⟩ orientation in the build direction is discussed here.

The melt pool shape, which largely determines the thermal gradient direction (i.e., normal to the melt-pool edge), is important for texture formation. The shape of the melt-pool varied between the two specimens: near parabolic in the specimen fabricated under lower energy density (with CLM), and near keyhole under higher energy density (with single-crystalline-like texture). This suggests the melting mode differed: conduction mode at lower energy density, and keyhole mode at higher energy density [15]. The migration of the solid–liquid interface varies depending on the melting mode of the melt-pool. In the conduction mode (Fig. 4(a)), the curvature of the melt-pool bottom decreases during solidification, and the migration of the solid–liquid interface is frequently toward the build direction as solidification proceeds [16]. In contrast, the curvature of melt-pool bottom has been reported to increase as solidification proceeds in the keyhole mode [17,18], indicating that lateral migration of the solid–liquid interface is dominant at the melt-pool bottom (Fig. 4(b)).

With regard to the specimen fabricated under lower energy density (with CLM), the directions of the thermal gradient and solid–liquid interface migration tend to be parallel to the build direction, which is preferable for forming columnar cells along the build direction. Once the vertically grown columnar cells are formed, the orientation is easily inherited through epitaxial growth [7,8]. The elongated-cell direction corresponds to ⟨001⟩, which is the easy-growth direction of cubic materials. Therefore, ⟨001⟩-oriented minor layers develop between the ⟨011⟩-oriented major layers, forming a CLM.

On the other hand, in the specimen fabricated under higher energy density (with single-crystalline-like texture), lateral migration of the solid–liquid interface might be dominant. There would be little chance for cells to grow along the build direction at the bottom of the melt-pool. If vertically grown cells form by chance, their growth will be stopped by lateral solid–liquid interface migration. Fragments with ⟨001⟩ orientation along the build direction were partly observed in the lower part of the specimen fabricated under higher energy density; however, they did not extend through multiple melt-pools (Supplementary Fig. 3). Hence, minor layers do not form at this higher energy density, generating a single-crystalline-like texture.

In this study, we concentrated only on the mechanism of CLM development in 316L stainless steel by the X-scan strategy using SLM. The development of CLM simultaneously improved the mechanical properties and corrosion resistance compared to commercially obtained specimens. This finding should be applicable to other materials by appropriate parameter control in the fabrication process. We will further examine the mechanism of the improvement of the mechanical and corrosion properties by the CLM: with regard to the mechanical properties, the continuity of the deformation (strain) between the major and minor layers must be important; and for the corrosion properties, the

Table 1
Mechanical properties of SLM-built specimens and commercial reference specimen.

	SLM-CLM	SLM-Single	Reference specimen	*P* value (CLM vs single)
Yield stress (MPa)	387 ± 11[a]	346 ± 6[a]	238 ± 6	<0.05
Ultimate tensile strength (MPa)	924 ± 29	921 ± 19	950 ± 4	>0.05 (NS)
Elongation (%)	67.5 ± 0.9[a]	69.9 ± 2.6[a]	59.8 ± 0.2	>0.05 (NS)

NS: not significant.
[a] $P < 0.05$ vs reference.

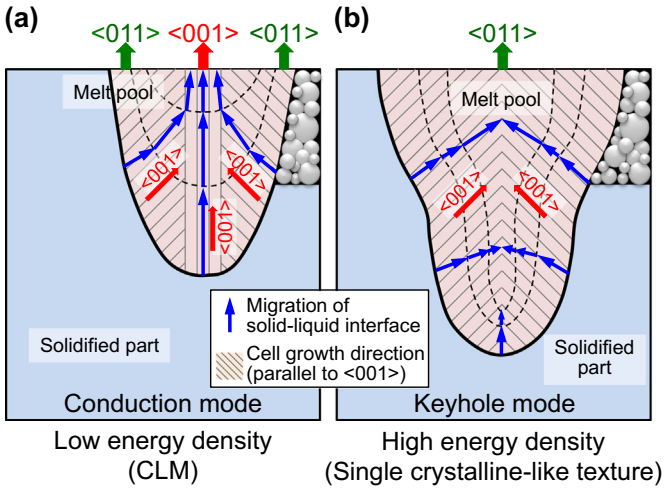

Fig. 4. Schematic illustration depicting the migration of the solid–liquid interface during melt-pool solidification under (a) low energy density (conduction mode) and (b) high energy density (keyhole mode). In the conduction mode, the melt-pool bottom becomes flat, so that the solid–liquid interface frequently migrates along the build direction, which develops ⟨001⟩-oriented columnar cells along the build direction in the melt-pool center.

minimization of the precipitated manganese sulfide inclusion in the SLM process, which acts as the initiation site of the localized corrosion, and its orientation dependence should be focused on. The details of these will be described elsewhere.

Declarations of interest

None.

Acknowledgements

This work was supported by the Council for Science, Technology and Innovation (CSTI), the Cross-Ministerial Strategic Innovation Promotion Program (SIP), and Innovative design/manufacturing technologies (Establishment and Validation of the Base for 3D Design & Additive Manufacturing Standing on the Concepts of Anisotropy & Customization) from the New Energy and Industrial Technology Development Organization (NEDO). This work was also supported by Grants-in-Aid for Scientific Research from the Japan Society for Promotion of Science (grant numbers JP18H05254 and JP18H03844), and 2018 Research Promotion Grant from Iron and Steel Institute of Japan (ISIJ).

Appendix A. Supplementary data

Supplementary data to this article can be found online at https://doi.org/10.1016/j.scriptamat.2018.09.017.

References

[1] G.P. Dinda, A.K. Dasgupta, J. Mazumder, Scr. Mater. 67 (2012) 503–506.
[2] L. Thijs, M.L.M. Sistiaga, R. Wauthle, Q. Xie, J.P. Kruth, J. Van Humbeeck, Acta Mater. 61 (2013) 4657–4668.
[3] R.R. Dehoff, M.M. Kirka, W.J. Sames, H. Bilheux, A.S. Tremsin, L.E. Lowe, S.S. Babu, Mater. Sci. Technol. 31 (2015) 931–938.
[4] H. Helmer, A. Bauereiß, R.F. Singer, C. Körner, Mater. Sci. Eng. A 668 (2016) 180–187.
[5] F. Geiger, K. Kunze, T. Etter, Mater. Sci. Eng. A 661 (2016) 240–246.
[6] K. Hagihara, T. Nakano, M. Suzuki, T. Ishimoto, S.H. Suyalatu, J. Sun, Alloys Compd. 696 (2017) 67–72.
[7] T. Ishimoto, K. Hagihara, K. Hisamoto, S.H. Sun, T. Nakano, Scr. Mater. 132 (2017) 34–38.
[8] S.H. Sun, K. Hagihara, T. Nakano, Mater. Des. 140 (2018) 307–316.
[9] T.P. Gabb, J. Gayda, R.V. Miner, Metall. Mater. Trans. A 17 (1986) 497–505.
[10] V. Sass, U. Glatzel, M. Feller-Kniepmeier, Acta Mater. 44 (1996) 1967–1977.
[11] Y. Umakoshi, T. Nakano, ISIJ Int. 32 (1992) 1339–1347.
[12] T. Nakano, K. Hagihara, Y. Nakai, Y. Umakoshi, Intermetallics 14 (2006) 1345–1350.
[13] M. Todai, T. Nakano, T. Liu, H.Y. Yasuda, K. Hagihara, K. Cho, M. Ueda, M. Takeyama, Addit. Manuf. 13 (2017) 61–70.
[14] G. Sander, S. Thomas, V. Cruz, M. Jurg, N. Birbilis, X. Gao, M. Brameld, C.R. Hutchinson, J. Electrochem. Soc. 164 (2017) C250–C257.
[15] W.E. King, H.D. Barth, V.M. Castillo, G.F. Gallegos, J.W. Gibbs, D.E. Hahn, C. Kamath, A.M. Rubenchik, J. Mater. Process. Technol. 214 (2014) 2915–2925.
[16] C. Zhao, K. Fezzaa, R.W. Cunningham, H. Wen, F. De Carlo, L. Chen, A.D. Rollett, T. Sun, Sci. Rep. 7 (2017) 3602.
[17] W.I. Cho, S.J. Na, C. Thomy, F. Vollertsen, J. Mater. Process. Technol. 212 (2012) 262–275.
[18] S.A. Khairallah, A.T. Anderson, A. Rubenchik, W.E. King, Acta Mater. 108 (2016) 36–45.